Geophysical Journal International

Geophys. J. Int. (2025) **242,** 1–17
Advance Access publication 2025 January 06
Research Paper

https://doi.org/10.1093/gji/ggaf002

Unveiling GRACE-based estimation techniques: insights from multichannel singular spectrum analysis of geocentre motion

Hongjuan Yu,[1] Yong Zhang,[1] Yu Sun [2] and Krzysztof Sośnica[3]

[1] *School of Geomatics, Liaoning Technical University, Fuxin* 123000*, China. E-mail: yuhongjuan123@163.com*
[2] *Key Lab of Spatial Data Mining and Information Sharing, Ministry of Education, Fuzhou University, Wulongjiang North Road, Fuzhou* 350108*, Fujian, China. E-mail: jade.yusun@outlook.com*
[3] *Institute of Geodesy and Geoinformatics, Wrocław University of Environmental and Life Sciences, Grunwaldzka* 53*,* 50-357 *Wrocław, Poland*

Accepted 2024 December 30. Received 2024 December 30; in original form 2024 July 27

SUMMARY

This study aims to provide valuable scientific insights into various estimation techniques of geocentre motion (GCM) from the perspective of signal analysis, thereby enhancing Gravity Recovery and Climate Experiment (GRACE) users' understanding and application of GCM. Initially, it utilizes the satellite laser ranging (SLR) technique with the network shift approach to estimate over 30 yr of weekly GCM time-series from 1994 to 2024. Subsequently, we employ two approaches to estimate three types of monthly GCM time-series spanning more than 20 yr from 2002 to 2023: combining GRACE data with an ocean bottom pressure model (GRACE-OBP approach), the fingerprint approach (FPA), and the fingerprint approach with satellite altimetry data (FPA-SA, up to 2022). The former is referred to as SLR-based GCM estimates, while the latter, which uses GRACE Earth's gravity field models, is termed GRACE-based GCM estimates. Furthermore, this study pioneers the use of multichannel singular spectrum analysis (MSSA) for GCM analysis, especially focusing on the latest GRACE-based GCM estimates from the GRACE-OBP and FPA/FPA-SA approaches, marking the first comprehensive analysis of GCM estimated by various techniques. The results show that MSSA can effectively extract common signals from the three components of the GCM time-series. The seasonal components extracted from GRACE-based GCM estimates using MSSA are consistent with those from SLR-based GCM estimates, although the former exhibit slightly larger amplitudes of the annual and semi-annual signals. After correcting the atmosphere-ocean dealiasing, the amplitudes of the SLR-based estimates correspondingly decrease, remaining slightly larger but becoming closer to those of the GRACE-based estimates. However, a periodic signal with an approximate 160-d period is detectable in all GRACE-based GCM estimates, but it is absent in SLR-based GCM estimates. Further investigation using MSSA into higher degree spherical harmonic (SH) coefficients of the Earth's gravity field models reveals that these SH coefficients contain a 160-d periodic signal. This finding suggests that the signal detected in GRACE-based GCM estimates originates from systematic errors in these SH coefficients, offering new insights for improving the accuracy of GRACE Earth's gravity field solutions. Additionally, GRACE-based GCM estimates show significant secular non-zero trends, notably larger than those in SLR-based GCM estimates, which are not expected to exhibit any trends. However, the reliance of GRACE-based GCM estimates on geophysical models (e.g. glacier melting, glacial isostatic adjustment and hydrological models) limits the accuracy of their trends, underscoring the need for further validation. Overall, this study highlights new challenges regarding the accuracy of GRACE-based GCM estimates and emphasizes the necessity for further validation in mass change research.

Key words: Reference systems; Satellite geodesy; Satellite gravity; Time variable gravity; Time-series analysis.

1 INTRODUCTION

Geocentre motion (GCM) refers to the displacement of the centre of mass (CM) of the entire Earth system relative to its centre of figure (CF; Dong *et al.* 1997; Chen *et al.* 1999; Zannat and Tregoning, 2017a), as illustrated in Fig. 1. GCM is primarily caused by mass redistribution due to factors, such as atmospheric circulation, hydrological load changes (Zhang *et al.* 2023), sea level rise (Bergmann-Wolf *et al.* 2014; Chen *et al.* 2020), and glacier melting (Dong *et al.* 1997; Chen *et al.* 1999; Zhang and Sun, 2018; Loomis *et al.* 2020). GCM not only reflects the complex mass redistribution processes within the Earth system (Guo *et al.* 2008; Chen *et al.* 2019) but also holds significant importance in geophysics, geodynamics and satellite navigation research. Quantifying and analysing GCM is crucial for establishing and maintaining an accurate International Terrestrial Reference Frame (ITRF) (Sosnica *et al.* 2014; Zajdel *et al.* 2019a), understanding climate change (Zhang & Sun 2018), and other space geophysical applications, particularly those involving the Gravity Recovery and Climate Experiment (GRACE) satellite mission (Chen *et al.* 2020; Chen *et al.* 2022).

Currently, the main methods for determining GCMs include the network shift approach, the dynamic approach, the GRACE-OBP approach, that is, combining GRACE data with an ocean bottom pressure model, and the fingerprint approach (FPA). This study focuses on all these primary methods of GCM estimation. The first two methods rely on the satellite laser ranging (SLR) technique, while the latter two utilize GRACE Earth's gravity field models and other geophysical models. In our study, we refer to them as SLR-based and GRACE-based GCM estimates, respectively.

In the dynamic approach (Ries 2016; Cheng 2024), non-zero degree-1 spherical harmonic (SH) coefficients are calculated with respect to the CF frame, as realized by the a priori ITRF (Métivier *et al.* 2020; Altamimi *et al.* 2023). The GCM can be determined from the degree-1 SH coefficients through a linear transformation. However, due to strong correlations between the SH coefficients, reliable estimations require combining data from multiple satellites with different inclinations. Additionally, the complexity associated with degree-1 SH coefficients, correlations with dynamical orbit parameters and non-inertial reference frames has limited the widespread use of this method.

The network shift approach (Sosnica *et al.* 2015; Yu *et al.* 2021) imposes minimal constraints using the 7-parameter Helmert minimum constraint conditions, which applies no-net-translation (NNT, three translation constraints), no-net-rotation (NNR, three rotation constraints), and no-net-scale (one scale constraint). These conditions ensure that station coordinates derived from satellite-based solutions are constrained in the CF frame. During SLR parameter estimation, the translation vector between the CF and CM frameworks is simultaneously estimated (Zajdel *et al.* 2019a) using the NNT constraint. Additionally, when determining Earth rotation parameters together with satellite orbits and station coordinates, NNR is also imposed on the core SLR network. In other words, the geocentre vector is directly treated as a parameter to be estimated, representing the translation of the origin (i.e. $\vec{r}_{\mathrm{GCM}}$ in Fig. 1). In other network shift approaches (Spatar 2016), station coordinates are first determined in the CM frame and then the Helmert transformation is applied to determine three translation parameters between the CM and CF frameworks letting satellites orbit around the CM and not the CF.

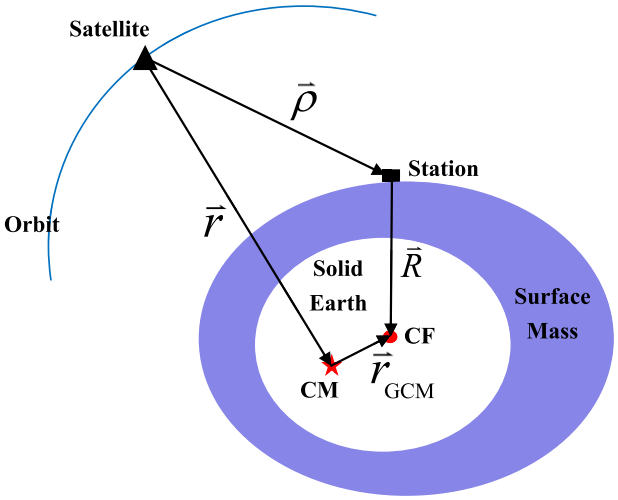

Figure 1. The relationship between CM and CF.

The GRACE-OBP approach has undergone continuous development. Initially, Swenson *et al.* (2008) estimated a time-series of geocentre anomalies using data from the GRACE satellite mission combined with the output from an ocean model. Since then, this method has been optimized for estimating GCMs (Sun *et al.* 2016a) and the variations in the C_{20} (Sun *et al.* 2016b, 2017) and C_{30} (Sun *et al.* 2023) coefficients. This optimization combines GRACE mission data with an OBP model and a glacial isostatic adjustment (GIA) model (Peltier *et al.* 2018), while simultaneously accounting for self-attraction and loading effects. This approach is particularly beneficial for GRACE users as it allows for the estimation of degree-1 mass coefficients that are compatible with the higher-degree SH coefficients provided by the GRACE mission (Sun *et al.* 2023).

The FPA approach (Sun *et al.* 2019) divides the Earth's surface into reasonable blocks and calculates the fingerprints of these blocks based on the sea level equation. This approach exclusively utilizes GRACE data and the geoid fingerprints of mass redistributions occurring both at the surface and within the Earth's interior. By doing so, the FPA enables the determination of variations in the degree-1 Stokes and C_{20} coefficients of the Earth's gravity field induced by mass redistribution. It is also possible to incorporate satellite altimetry (SA) data into the FPA approach following Rietbroek *et al.* (2016), which can be referred to as FPA-SA.

Since the launch of the GRACE satellite in 2002 (Tapley *et al.* 2004) and its successor GRACE Follow On, GRACE missions have routinely produced high-precision, high-resolution monthly gravity field models. However, these models are limited by their inability to directly provide GCM estimates and feature low-precision coefficients for C_{20} and C_{30}. In previous studies (e.g. Nie *et al.* 2024), the GCM was generally replaced by the widely used GRACE-OBP GCM estimates (Swenson *et al.* 2008; Sun *et al.* 2016a). As recommended in Technical Note TN-14 (Loomis *et al.* 2019), the C_{20} coefficients in GRACE solutions should be replaced with those derived from SLR. Recent advancements in methods such as GRACE-OBP (Sun *et al.* 2016b, 2023) and FPA/FPA-SA (Sun *et al.* 2019) approaches now enable the simultaneous estimation of GCM, C_{20} and C_{30} coefficients. Current research recommends using GCM estimates from these three methods to replace the corresponding coefficients in GRACE solutions for improved consistency (Sun *et al.* 2023). FPA, in particular, can simultaneously estimate GCM and interpret it as induced by various individual sources (Sun *et al.* 2019).

Table 1. The information on the SLR-based GCM estimates

Name	Approach	Temporal resolution (d)	Time span
Yu-SLR-weekly	Network shift method	7	1994 Jan.–2024 Apr.
AIUB-SLR-weekly	Network shift method	7	1994 Jan.–2015 Jan.
CSR-SLR-monthly	Dynamic method	30	1994 Jan.–2023 Jun.
CSR-SLR-bimonthly	Dynamic method	60	1998 Feb.–2024 Apr.

However, GRACE-based approaches rely heavily on geophysical models and the reliability of these models significantly constrains the accuracy of GCM estimates. For instance, the GRACE-OBP method primarily depends on models of OBP and GIA, as well as higher degrees and orders of Earth's gravity field coefficients (i.e. C_{lm}/S_{lm} with $l \geq 2$ and for $l = 2$, $m \neq 0$). FPA calculates GCM and C_{20} variations by summing the contributions from various geophysical processes. Consequently, seasonal and interannual variations are modelled through the atmospheric, oceanic and terrestrial water storage models, while long-term trends depend on models of glacier melting and GIA (Sun *et al.* 2019). Therefore, high-degree Earth's gravity field models are necessary for these methods. Theoretically, the GRACE-OBP approach estimates degree-1 coefficients by combining higher-degree Earth's gravity field models with OBP models, employing a process similar to training higher-degree coefficients to deduce or refine degree-1 and C_{20} coefficients. In contrast, while the SLR technique is limited by uneven and sparse global station distribution (Glaser *et al.* 2019), which typically affects GCM through network effects (Zannat and Tregoning 2017b; Zajdel *et al.* 2019b), SLR-based estimates are grounded in actual satellite observations (Cheng *et al.* 2013a;b; Ries 2016; Kosek *et al.* 2020). As a result, GCMs based on direct observations are considered the most authentic and reliable for verifying and calibrating GRACE-derived products. Additionally, unlike GRACE-based approaches, SLR has been a proven geodetic technique capable of determining reliable GCM for over three decades since the launch of LAser GEOdynamics Satellite 2 (LAGEOS-2) in 1992 October, which is 10 yr longer than GRACE-based GCM, making it extremely valuable for analysing long-term time-series.

In terms of signal analysis, one of the main advantages of multichannel singular spectrum analysis (MSSA) over singular spectrum analysis (SSA; Hassani 2007) is its ability to analyse multiple time-series simultaneously (Ji *et al.* 2023), whereas SSA typically focuses on a single time-series. MSSA expands on the capabilities of SSA by effectively dealing with multivariate data, enhancing signal extraction, and providing insights into the interrelationships among the X, Y and Z components of the GCM. Yu *et al.* (2021) used SSA to separate geophysical signals in the LAGEOS GCM from 1994 to 2020, but they were unable to extract common signals across the X, Y and Z components. Furthermore, despite extensive research on GCM, significant differences in time-series analysis results persist due to variations in estimation methods and temporal resolutions. Certain periodic signals in GCM time-series, estimated using different technical approaches, remain inadequately explained, highlighting the need for further analysis of their origins.

This study investigates five types of GCM time-series estimated by commonly employed methods and subsequently analyses these long-term GCM time-series at different temporal resolutions. Specifically, this study estimates four types of GCM time-series, while one time-series is provided by the Center for Space Research (CSR; Ries 2016). Given that satellite altimetry products are available only up to 2022, the FPA-SA-based GCM estimates also extend only up to 2022. In addition, we analyse the SLR weekly estimates for more than 30 yr, from 1994 to the present (Yu *et al.* 2021), monthly estimates from 1994 to 2023 (Ries 2016) and detrended bimonthly estimates covering approximately 27 yr, from 1998 to the present (Ries 2016). Detailed information can be found in Table 1.

This study aims to provide valuable insights into various estimation techniques for GCM through a comprehensive analysis from both estimation and signal analysis perspectives. It serves as a thorough reference for GRACE users to enhance their understanding and application. Additionally, it pioneers the use of MSSA for GCM analysis, particularly focusing on the latest GCM estimates from the GRACE-OBP and FPA/FPA-SA approaches, marking the first in-depth study of GCM estimates derived from various methods.

The paper is structured as follows: Section 2 provides a brief overview of the GRACE-based GCM estimation theory and MSSA theory, while Section 3 calculates the GCM estimates and conducts a comparative analysis. Section 4 employs MSSA to study the GCM estimates from different approaches. Finally, Section 5 presents the conclusions.

2 METHODOLOGY

In this paper, we calculate four types of GCM time-series. One series is based on the network shift approach, while the other three utilize GRACE-based methods. Both the network shift (Yu *et al.* 2021) and CSR's dynamic method (Ries 2016) rely on LAGEOS1/2 satellite observation data. Our primary focus is on analysing issues related to GCM time-series derived from GRACE-based methods, so we briefly outline the principles of GRACE-OBP and FPA/FPA-SA to facilitate subsequent problem analysis. Additionally, since our analysis primarily employs MSSA, we provide a concise explanation of its principles.

2.1 GRACE-OBP

The GRACE satellites orbit around the CM, which sets the degree-1 SH coefficients to zero by definition. Swenson *et al.* (2008) estimated degree-1 coefficients by combining GRACE data with outputs from an OBP model. They demonstrated that, with knowledge of the oceanic degree-1 coefficients, it is possible to derive the full degree-1 coefficients (see their eq. 12). Sun *et al.* (2016b) further refined this method by incorporating self-gravitation and loading effects to better account for water exchange between land and oceans. The degree-1 coefficients obtained through this method will be referred to as GRACE-OBP degree-1 coefficients. For further details, please refer to Swenson *et al.* (2008) and Sun *et al.* (2016b).

2.2 FPA

The FPA (Rietbroek *et al.* 2016; Sun *et al.* 2019) divides regions with significant mass change at the Earth's surface into subregions,

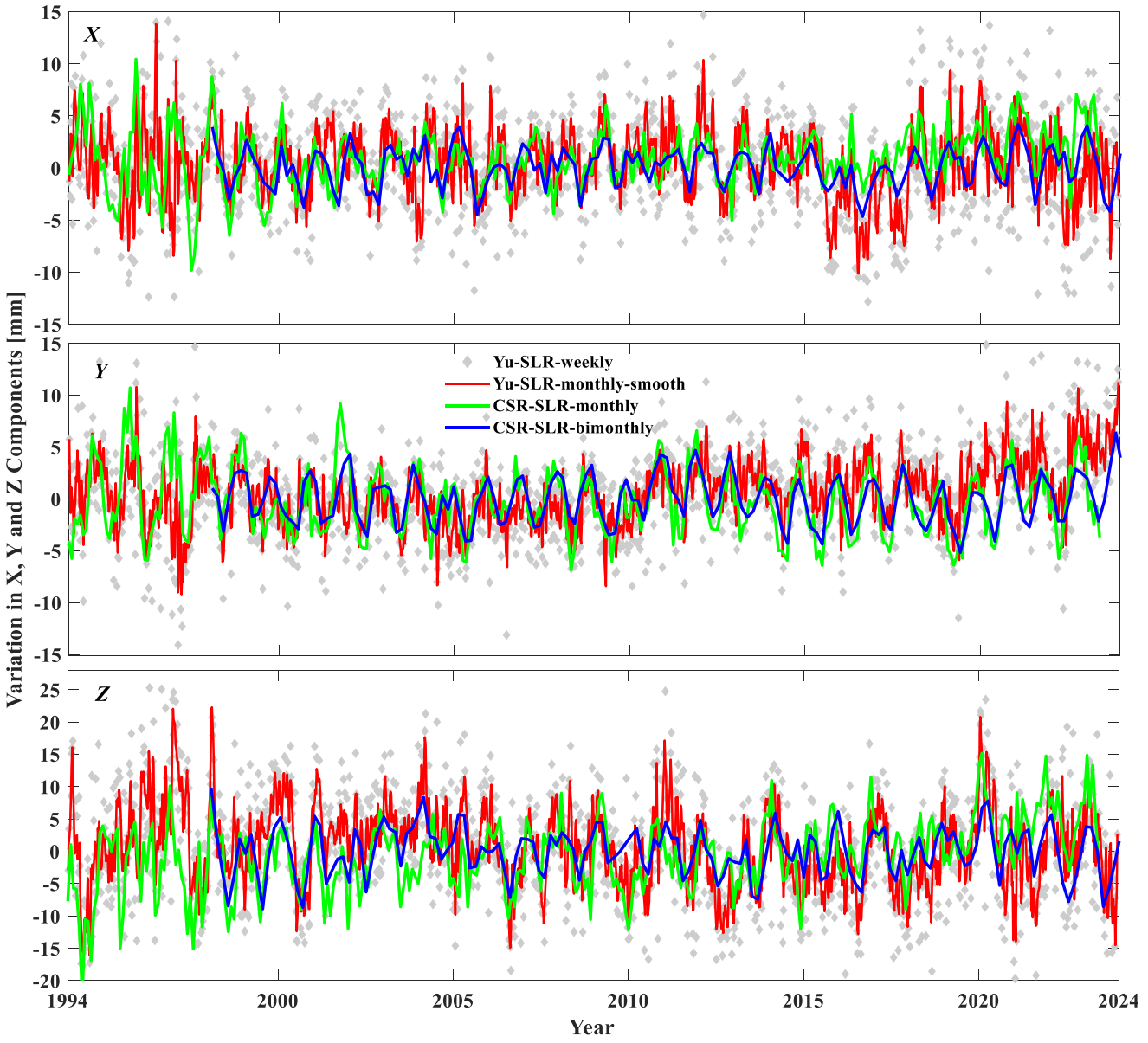

Figure 2. SLR-based GCM time-series with different processing schemes. Yu-SLR-monthly smooth was derived from the Yu-SLR-weekly time-series after applying smoothing with a 1-month window.

each with prescribed mass change patterns normalized to one gigaton. These mass-change regions are defined in the CF reference frame, meaning each has its own degree-1 coefficients. Fingerprints for each mass-change block are then calculated using the sea level equation (Tamisiea *et al.* 2010). The weighted sum of all fingerprints is expected to match the observed GRACE gravity changes, excluding degree-1 coefficients, under the assumption that the designated mass changes are sufficiently representative. With this constraint, weights for each fingerprint can be derived, enabling the estimation of the full degree-1 coefficients, referred to here as the FPA degree-1 coefficients.

In addition to GRACE data, the gravity field predicted by the weighted sum of fingerprints can also be constrained by other geodetic techniques, such as SA. The degree-1 coefficients derived from this combined approach will be referred to as degree-1 coefficients from the FPA-SA method. For further details, readers are referred to Rietbroek *et al.* (2016) and Sun *et al.* (2019).

2.3 MSSA

MSSA enables the simultaneous analysis of multiple time-series compared to SSA, enhancing signal extraction and uncovering the interrelationships among different components in the GCM time-series. The process involves constructing a lag trajectory matrix and a Toeplitz lag-covariance matrix, followed by singular value decomposition to reconstruct the principal components, which facilitates the identification of trends and periodic signals (Zhou

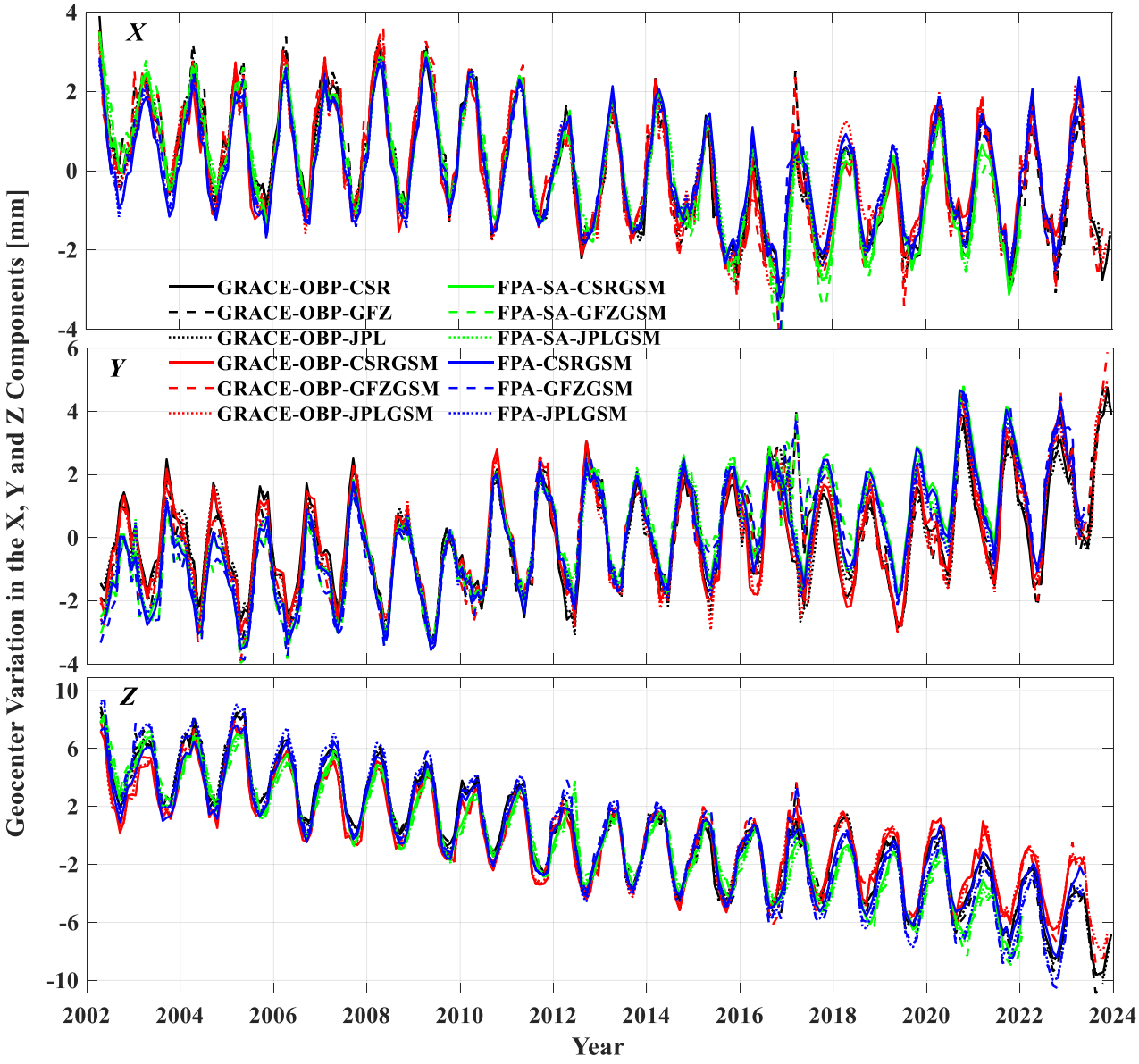

Figure 3. GRACE-based GCM time-series with different processing schemes.

et al. 2020; Jin *et al.* 2021; Shen *et al.* 2021; Wang *et al.* 2021; Ji *et al.* 2023).

3 GEOCENTRE MOTION SOLUTIONS AND COMPARISON

3.1 SLR-based GCM estimates

We utilize the solution strategy from Yu *et al.* (2021) to compute the weekly GCM time-series based on observations from the LAGEOS-1 and LAGEOS-2 satellites, covering over 30 yr from 1994 to the present. Additionally, we obtain two other GCM time-series with monthly and bimonthly solutions from Ries (2016) of CSR, available on the website (https://filedrop.csr.utexas.edu/pub/slr/geocenter/). These three SLR-based GCM estimates include the full signal because no atmosphere-ocean dealiasing (AOD-1B) component has been removed. In subsequent GRACE solutions, the ocean and atmospheric components are reduced by the AOD products (ftp://isdcftp.gfz-potsdam.de/grace-fo/Level-1B/GFZ/AOD/). To achieve full consistency, AOD corrections are also applied to the Yu-SLR-weekly GCM solutions. Additionally, a shorter AOD-corrected GCM time-series from the Astronomical Institute of the University of Bern (AIUB) is available at http://ftp.aiub.unibe.ch/GRAVITY/GEOCENTER (Sosnica *et al.* 2015). To maintain the originality of the monthly and bimonthly GCM estimates from CSR and to facilitate comparisons with the AOD-corrected GCM estimates, no additional AOD corrections will be applied, referred to as 'w/o AOD-1B'. We perform a comparative analysis of the SLR-based GCM time-series across different temporal resolutions, with detailed information about these four series provided in Table 1.

Fig. 2 shows the SLR-based GCM time-series for the *X*, *Y* and *Z* components. The time-series derived from various SLR processing schemes display minimal differences. However, the solutions by Yu

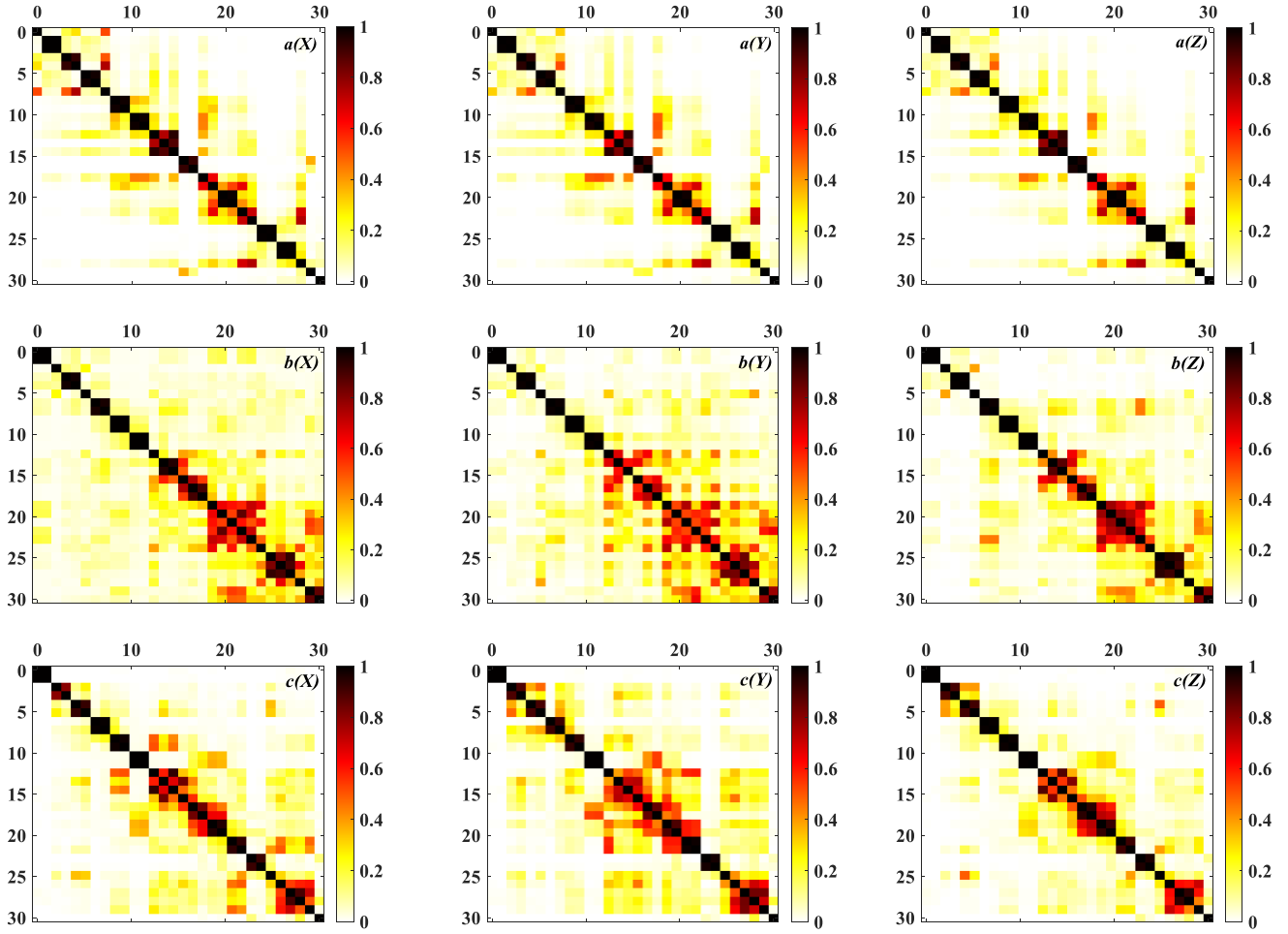

Figure 4. The first 30 w-correlations of reconstructed components of the SLR-based GCM *X*, *Y* and *Z* components from weekly (a), monthly (b) and bimonthly (c) solutions.

et al. (2021), show more pronounced high-frequency signals due to their higher temporal resolution. Additionally, the monthly GCM time-series from CSR indicates an upward trend in the Z component after 2017. Overall, the changes in trend for the SLR-based GCM estimates are relatively small.

3.2 GRACE-based GCM estimates

We employed two approaches, GRACE-OBP and FPA, to calculate three types of GRACE-based GCM time-series. All three GCM estimates utilize the level-2 RL06.1 and RL06.2 data sets (denoted as GSM, which is the Product Identifier mnemonic of the level-2 products from GRACE and GRACE-FO missions), released by the official agencies: CSR, GeoForschungsZentrum (GFZ), and Jet Propulsion Laboratory (JPL). The AOD-1B component has been removed from the GRACE-based GCM estimates. The time span for the GRACE-OBP and FPA approaches extends from 2002 April to either 2023 May or November, as the GSM solution is available only until that time, with truncation degrees ranging from 1 to 60. The GIA model (Peltier *et al.* 2018) is used to remove long-term solid Earth signals. Since the satellite altimetry product is only available up to 2022 January, the time span for FPA-SA estimates is from 2002 April to 2022 January.

The GRACE Level-2 RL06.1 and RL06.2 data sets provided by CSR, GFZ, and JPL contain 33 missing data points, making the intermittent time-series unsuitable for GCM studies. To further investigate GCMs, we will apply iterative interpolation along with SSA to fill these gaps (Wang *et al.* 2021; Ji *et al.* 2023). Identifying the timestamps of the missing data is a crucial first step in understanding the GCM coverage derived from the GRACE-OBP and FPA/FPA-SA approaches. Prior to 2016, data gaps typically lasted one or two months. However, between 2017 and 2018, there was an extended gap of 11 months.

The interpolated time-series were used to better represent the GCM variations in the *X*, *Y* and *Z* components. Based on GRACE Level-2 RL06.1 and RL06.2 gravity field models, we calculated the GCM time-series from 2002 to 2023 using the GRACE-OBP and FPA/FPA-SA approaches. To verify the accuracy of our GCM estimates, we also included the estimates calculated using the GRACE-OBP approach from CSR, GFZ and JPL. A total of 12 GCM time-series are illustrated in Fig. 3. Due to significant differences between the trends of SLR-based and GRACE-based GCM estimates, they are presented in separate figures.

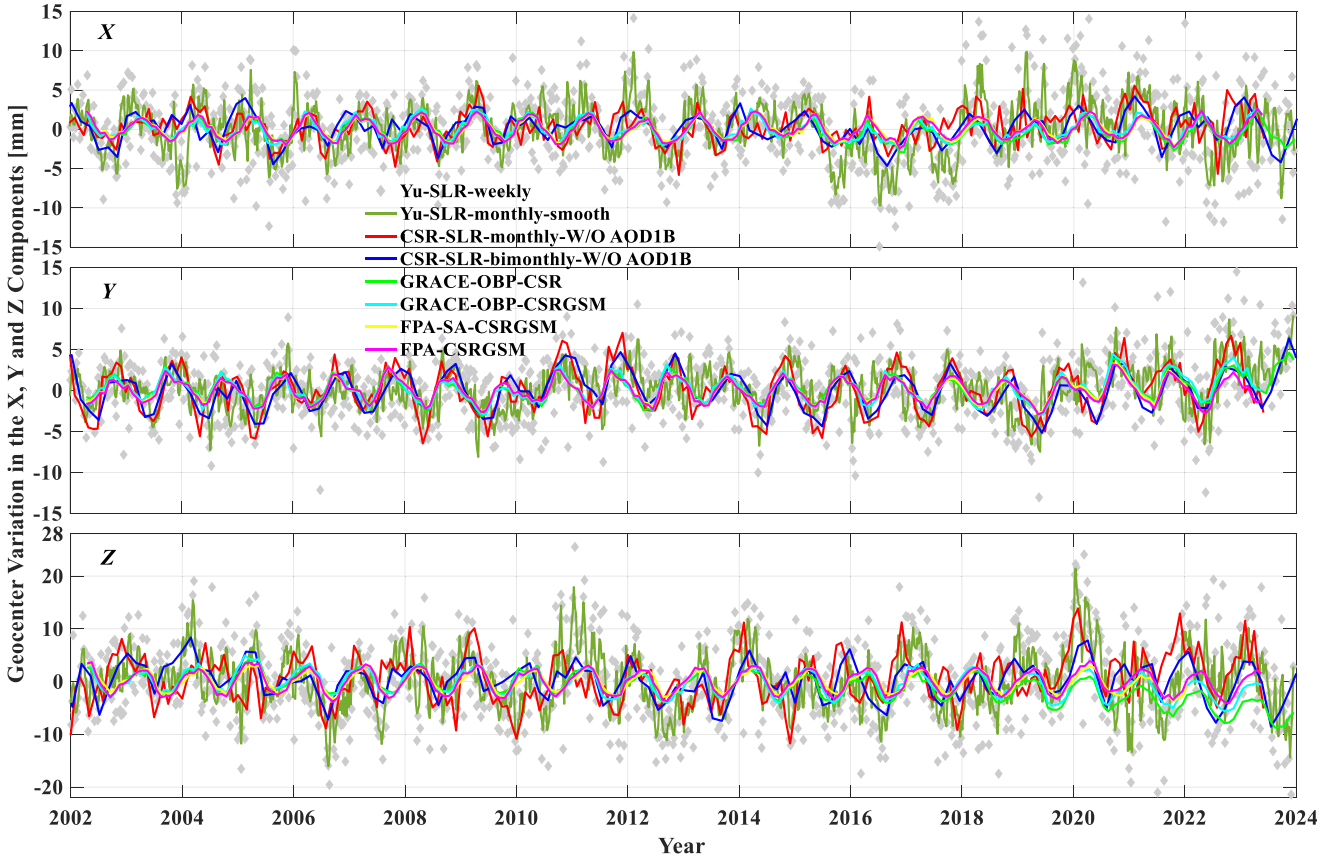

Figure 5. Detrended SLR-based and GRACE-based GCM time-series.

These GRACE-based GCM estimates show strong consistency, with only minor differences. The X component of the GCM is relatively stable but exhibits a slight negative trend, with deviations remaining within a few millimeters. This stability can be attributed to the X component pointing towards the prime meridian, primarily over the ocean, where mass variations are relatively stable, resulting in minimal trend changes. The Y component shows a trend towards the positive axis, with deviations similar to those of the X component. While the Y component remains relatively stable before 2010, the trend becomes more pronounced afterwards. The Z component of the GCM shows a significant negative trend, which is more pronounced than that of the X component. This trend mainly reflects the imbalance in melting rates between the Northern and Southern Hemispheres and is largely influenced by the Antarctic Ice Sheet (AIS). Over the past 20 yr, the impact of the Greenland Ice Sheet (GrIS) has been more significant than that of the AIS (Sun *et al.* 2019). However, the currently short time-series, limited polar region data in geophysical models, and the inherent limitations of glacier and GIA models make detecting long-term trend changes with high-accuracy challenging.

Comparing the GCMs derived from different approaches used in this study, the GRACE-OBP estimates from CSR, GFZ and JPL reveal a good consistency across all three components of the time-series, with only minor millimeter-level differences and occasional abrupt changes observed between 2016 and 2017. This consistency underscores the reliability of the GCM time-series estimated in this study. Additionally, our findings show that the trends in the *X* and *Y* components of the GCM remained relatively stable before 2010 but became more pronounced afterwards. These offsets may be attributed to issues with satellite accelerometers, different procedures of data screening, and differences in geophysical models or factors, though a definitive explanation remains unclear. For the Z component, a notable downward trend appears around 2007, which aligns well with mass changes in the AIS (Loomis *et al.* 2019, 2020). Moreover, the GRACE-based GCM estimates exhibit notably larger trends compared to SLR-based GCM estimates, emphasizing the considerable influence of factors such as AIS mass changes and the accuracy of the GIA model on the Z-component trend, which presents notable constraints.

In summary, compared to SLR-based GCM estimates, GRACE-based GCM estimates are more dependent on geophysical models. Apart from the Earth's gravity field models, they rely heavily on models such as the OBP model, and most notably, the GIA and glacier melting models, which exert a significant influence on the observed trends. The accuracy of these models, particularly the GIA model, imposes severe constraints on the precision of GCM estimates, which has profound implications for climate and geophysical studies, especially when these GCM estimates are used to replace degree-1 Stokes coefficients (i.e. GCM) in GRACE products.

4 GCM MSSA

4.1 W-correlation analysis of MSSA

The main objective of this study is to use MSSA to separate and extract the principal component signals from the

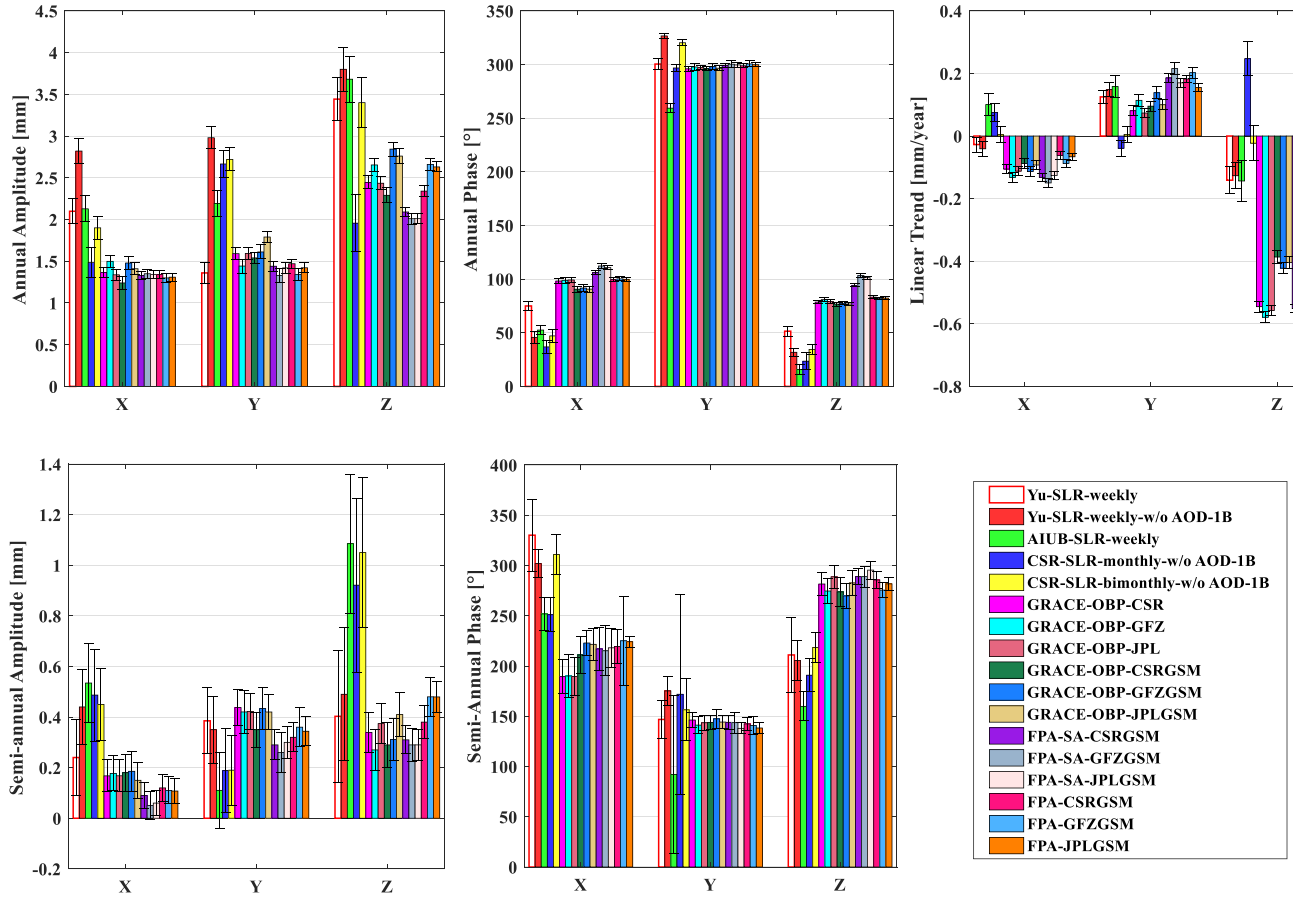

Figure 6. The GCM time-series with different processing schemes.

GCM time-series, investigate their temporal scale characteristics and thereby, further evaluate the advantages and disadvantages of different techniques and approaches for estimating GCM.

One of the main advantages of MSSA lies in its capacity to separate common seasonal signals, trend components and noise from multichannel time-series. In this study, we analyse the SLR-based and GRACE-based GCM time-series and employ w-correlation (Hassani 2007) to evaluate the effectiveness of different signal separations. A w-correlation exceeding 80 per cent indicates the same periodic components. When a reconstructed component is isolated, it represents a trend component, whereas paired components indicate periodic signals. The selection of the window is designed to optimize signal separation and is adjusted according to the characteristics of the GCM time-series. The differences in window length and the time-series characteristics directly affect the quality of signal separation. Typically, the optimal window length is an integer multiple of the annual signal period (Hassani 2007). The results demonstrate that the optimal window lengths for GCM time-series, calculated using the same method, are uniform across different cases.

Taking the SLR-based GCM estimates as an example, Figs 4(a)–(c) display the w-correlations of the reconstructed components for weekly, monthly and bimonthly SLR-based GCM estimates, respectively, with optimal window lengths of 4, 6 and 9 yr, respectively. While similarities between the GRACE-based and SLR-based GCM estimates are not shown individually, it is evident that the signal separation quality of the GRACE-based GCM estimates is inferior to that of the SLR-based estimates. This discrepancy can be attributed to uncertainties in the geophysical models underlying GRACE-based GCM estimates, including the high noise levels in GRACE data, particularly residual north–south striping errors at shorter timescales, and the limited temporal and spatial resolution, which restricts the detection of short-term or small-scale signals. Additionally, the complexity of estimating GCMs using GRACE data can result in signal loss or confusion, ultimately reducing the effectiveness of signal separation. The weekly GCM estimates show superior signal separation characteristics compared to the monthly and bimonthly estimates, indicating that the higher temporal resolution enhances MSSA's ability to separate and extract periodic signals. For example, Yu *et al.* (2021) detected periodic signals of 14 and 15 d that were not detectable at the monthly resolution from CSR.

4.2 Seasonal GCM analysis

Due to the different trends between SLR-based and GRACE-based GCM estimates, direct comparison is not feasible. Therefore, we chose the GRACE-centred GCM estimates (e.g. CSR) and compared them with the detrended SLR-based GCM estimates, as shown in Fig. 5. The overall variations in these GCM time-series are highly

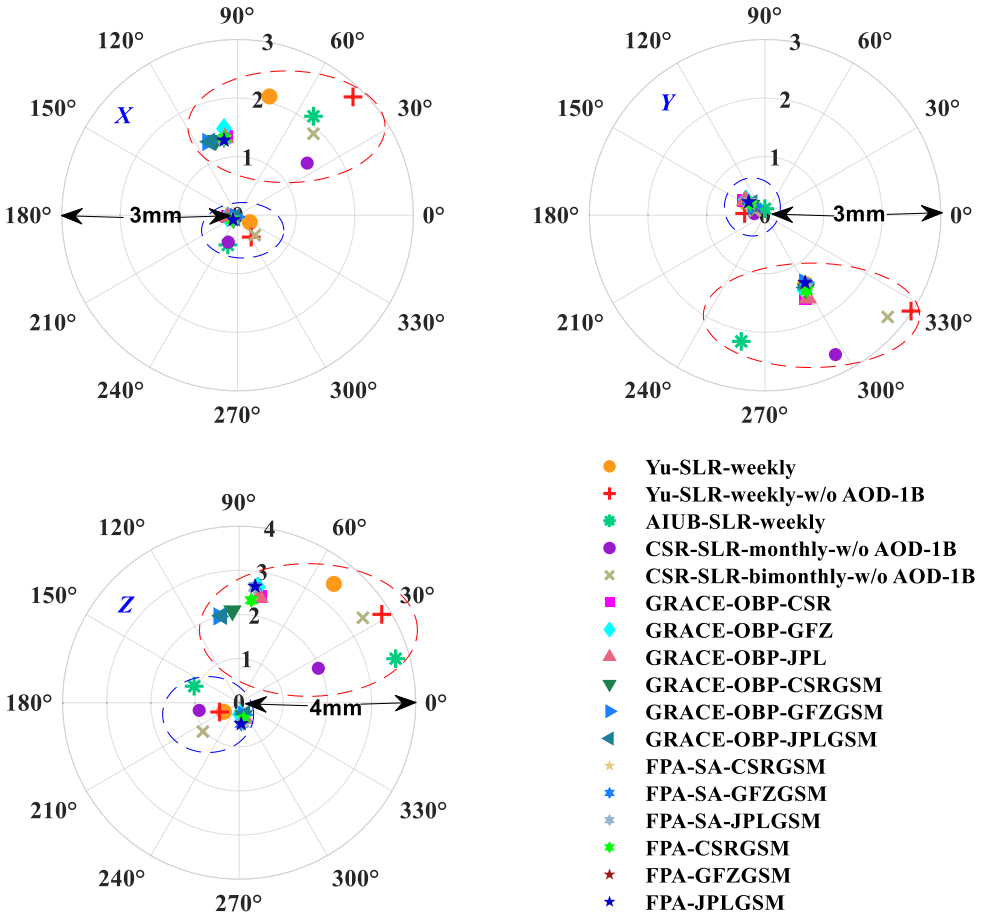

Figure 7. The phasor diagrams with phases and amplitudes of the annual (inside the large dashed circle) and semi-annual (inside the small dashed circle) signals in the GCM time-series.

consistent, although the fluctuations in the Yu-SLR-weekly GCM estimates are slightly increased.

The GCM time-series reveals significant seasonal signals, particularly annual and semi-annual signals, which are clearly detected in both SLR-based and GRACE-based GCM estimates. Detailed information about these seasonal signals and the linear trends of the SLR-based and GRACE-based GCM estimates is provided in Table 2 and illustrated in Fig. 6, facilitating the analysis of their seasonal characteristics across different approaches. In the *X*, *Y* and *Z* components, the mean annual amplitudes of the SLR-based GCM estimates are 1.90, 2.23 and 3.12 mm, while those for the GRACE-OBP, FPA-SA and FPA estimates are [1.39, 1.34, 1.31] mm, [1.60, 1.40, 1.41] mm, and [2.57, 2.04, 2.54] mm, respectively. The annual signal amplitudes of GRACE-based estimates are smaller than those of the SLR-based estimates, with GRACE-OBP estimates slightly exceeding the FPA estimates and aligning more closely with the SLR-based estimates. Additionally, the SLR-based semi-annual signal amplitudes are generally larger, except in the *Y* component, where they are smaller than the GRACE-OBP estimates.

In Fig. 6, the annual signals in the SLR-based GCM estimates are slightly larger than those in the GRACE-based estimates. Additionally, while the SLR-based GCM estimates show a consistency in the *Y* component, slight differences are evident in the *X* and *Z* components, particularly between the SLR-based weekly and monthly GCM estimates. In contrast, the annual signals among different GRACE-based GCM estimates show minimal differences and are generally consistent. The semi-annual signals of the SLR-based GCM estimates in the *Y* component are highly consistent with those of the GRACE-based GCM estimates, while significant differences are observed in the *X* and *Z* components. Notably, the semi-annual amplitudes of the SLR-based GCM estimates are approximately twice that of the GRACE-based GCM estimates. Additionally, one key distinction is that GRACE-based approaches remove the AOD-1B component, whereas some SLR-based solutions retain the full signal without applying AOD-1B corrections in this study. This difference significantly influences the annual and semi-annual signals, probably resulting in the larger amplitudes observed in the SLR-based GCM estimates compared to the GRACE-based estimates. Comparing Yu-SLR-weekly AOD-corrected GCM estimates with the SLR-based AOD-uncorrected estimates reveals a decrease in the annual and semi-annual amplitudes after the AOD correction. However, the annual amplitudes of the Yu-SLR-weekly and AIUB-SLR-weekly estimates remain larger than those of the GRACE-based estimates, likely due to the higher sensitivity of SLR to low-degree signals.

Table 2. The linear trends, annual/semi-annual amplitudes and phases of the GCM estimates.

Component	Solutions	Annual (mm, °)		Semi-annual (mm, °)		Linear trend
		Amplitude	Phase	Amplitude	Phase	(mm yr^{-1})
X	Yu-SLR-weekly	2.09 ± 0.15	74.98 ± 3.80	0.24 ± 0.15	330.16 ± 35.85	−0.027 ± 0.024
	AIUB-SLR-weekly	2.13 ± 0.16	52.51 ± 4.50	0.53 ± 0.16	251.82 ± 16.74	0.101 ± 0.036
	CSR-SLR-monthly w/o AOD-1B	1.48 ± 0.18	36.82 ± 6.32	0.49 ± 0.18	251.01 ± 16.84	0.075 ± 0.029
	CSR-SLR-bimonthly w/o AOD-1B	1.90 ± 0.14	47.07 ± 6.02	0.45 ± 0.14	310.82 ± 19.52	0.004 ± 0.026
	GRACE-OBP-CSR	1.37 ± 0.06	98.24 ± 2.35	0.17 ± 0.06	189.39 ± 16.89	−0.105 ± 0.014
	GRACE-OBP-GFZ	1.50 ± 0.07	98.89 ± 2.58	0.18 ± 0.07	190.10 ± 21.79	−0.132 ± 0.015
	GRACE-OBP-JPL	1.34 ± 0.06	99.22 ± 2.36	0.17 ± 0.06	189.60 ± 19.12	−0.112 ± 0.014
	GRACE-OBP-CSRGSM	1.24 ± 0.07	90.60 ± 2.90	0.18 ± 0.07	211.03 ± 18.66	−0.087 ± 0.016
	GRACE-OBP-GFZGSM	1.48 ± 0.08	91.66 ± 3.01	0.19 ± 0.08	222.89 ± 12.61	−0.113 ± 0.017
	GRACE-OBP-JPLGSM	1.41 ± 0.07	90.66 ± 2.73	0.15 ± 0.07	221.58 ± 15.94	−0.092 ± 0.015
	FPA-SA-CSRGSM	1.33 ± 0.05	99.61 ± 1.84	0.09 ± 0.05	219.49 ± 16.70	−0.062 ± 0.012
	FPA-SA-GFZGSM	1.35 ± 0.06	100.23 ± 1.95	0.05 ± 0.06	225.09 ± 43.99	−0.087 ± 0.012
	FPA-SA-JPLGSM	1.34 ± 0.05	99.82 ± 1.79	0.06 ± 0.05	224.15 ± 5.61	−0.066 ± 0.011
	FPA-CSRGSM	1.34 ± 0.05	106.20 ± 1.89	0.12 ± 0.05	216.98 ± 21.36	−0.132 ± 0.012
	FPA-GFZGSM	1.30 ± 0.05	112.24 ± 2.15	0.11 ± 0.05	215.15 ± 24.72	−0.150 ± 0.014
	FPA-JPLGSM	1.31 ± 0.05	110.71 ± 1.91	0.11 ± 0.05	218.09 ± 19.71	−0.126 ± 0.012
Y	Yu-SLR-weekly	1.35 ± 0.13	300.41 ± 5.07	0.38 ± 0.13	146.81 ± 19.35	0.125 ± 0.021
	AIUB-SLR-weekly	2.19 ± 0.15	296.78 ± 3.94	0.11 ± 0.15	92.11 ± 78.17	0.158 ± 0.035
	CSR-SLR-monthly w/o AOD-1B	2.67 ± 0.16	296.78 ± 2.89	0.19 ± 0.16	171.87 ± 99.31	−0.039 ± 0.026
	CSR-SLR-bimonthly w/o AOD-1B	2.72 ± 0.14	320.29 ± 2.56	0.19 ± 0.14	156.41 ± 30.91	0.005 ± 0.026
	GRACE-OBP-CSR	1.59 ± 0.07	296.02 ± 2.28	0.44 ± 0.07	146.25 ± 7.36	0.081 ± 0.015
	GRACE-OBP-GFZ	1.44 ± 0.08	297.73 ± 2.98	0.42 ± 0.08	141.19 ± 8.54	0.114 ± 0.019
	GRACE-OBP-JPL	1.59 ± 0.07	297.26 ± 2.27	0.42 ± 0.07	143.51 ± 7.26	0.074 ± 0.015
	GRACE-OBP-CSRGSM	1.54 ± 0.07	296.20 ± 2.13	0.35 ± 0.07	143.91 ± 6.98	0.096 ± 0.016
	GRACE-OBP-GFZGSM	1.61 ± 0.08	298.09 ± 2.71	0.43 ± 0.08	147.41 ± 9.19	0.138 ± 0.018
	GRACE-OBP-JPLGSM	1.79 ± 0.07	296.55 ± 2.11	0.42 ± 0.07	144.23 ± 6.78	0.100 ± 0.015
	FPA-SA-CSRGSM	1.44 ± 0.06	298.84 ± 1.86	0.29 ± 0.06	142.37 ± 6.39	0.182 ± 0.013
	FPA-SA-GFZGSM	1.33 ± 0.08	300.56 ± 2.72	0.26 ± 0.08	140.82 ± 8.62	0.202 ± 0.017
	FPA-SA-JPLGSM	1.42 ± 0.06	299.85 ± 1.20	0.30 ± 0.06	138.32 ± 5.02	0.155 ± 0.013
	FPA-CSRGSM	1.47 ± 0.06	299.02 ± 2.04	0.32 ± 0.06	143.97 ± 7.13	0.186 ± 0.015
	FPA-GFZGSM	1.34 ± 0.08	300.33 ± 3.02	0.36 ± 0.08	143.63 ± 10.56	0.216 ± 0.019
	FPA-JPLGSM	1.42 ± 0.06	299.60 ± 2.18	0.34 ± 0.06	137.98 ± 5.52	0.167 ± 0.015
Z	Yu-SLR-weekly	3.43 ± 0.26	51.44 ± 4.70	0.40 ± 0.26	210.99 ± 37.03	−0.141 ± 0.042
	AIUB-SLR-weekly	3.68 ± 0.27	15.73 ± 4.29	1.09 ± 0.27	159.85 ± 14.53	−0.144 ± 0.064
	CSR-SLR-monthly w/o AOD-1B	1.96 ± 0.34	23.51 ± 7.72	0.92 ± 0.34	190.86 ± 16.56	0.247 ± 0.055
	CSR-SLR-bimonthly w/o AOD-1B	3.40 ± 0.30	34.46 ± 4.65	1.05 ± 0.30	218.51 ± 14.79	−0.023 ± 0.055
	GRACE-OBP-CSR	2.44 ± 0.08	78.60 ± 1.68	0.34 ± 0.08	281.58 ± 11.46	−0.545 ± 0.017
	GRACE-OBP-GFZ	2.65 ± 0.08	80.87 ± 1.67	0.27 ± 0.08	274.61 ± 12.79	−0.579 ± 0.018
	GRACE-OBP-JPL	2.43 ± 0.08	79.14 ± 1.68	0.37 ± 0.08	288.74 ± 11.21	−0.557 ± 0.017
	GRACE-OBP-CSRGSM	2.29 ± 0.09	76.70 ± 1.83	0.29 ± 0.09	273.72 ± 14.49	−0.387 ± 0.020
	GRACE-OBP-GFZGSM	2.84 ± 0.08	77.50 ± 1.62	0.31 ± 0.08	269.72 ± 12.79	−0.422 ± 0.018
	GRACE-OBP-JPLGSM	2.76 ± 0.09	76.81 ± 1.77	0.41 ± 0.09	282.62 ± 12.78	−0.404 ± 0.019
	FPA-SA-CSRGSM	2.09 ± 0.05	83.19 ± 1.34	0.31 ± 0.05	285.61 ± 8.36	−0.480 ± 0.015
	FPA-SA-GFZGSM	2.01 ± 0.07	82.19 ± 1.13	0.29 ± 0.07	275.54 ± 7.24	−0.616 ± 0.014
	FPA-SA-JPLGSM	2.01 ± 0.06	82.33 ± 1.08	0.29 ± 0.06	281.73 ± 6.52	−0.613 ± 0.014
	FPA-CSRGSM	2.34 ± 0.07	94.17 ± 1.27	0.38 ± 0.07	288.90 ± 8.24	−0.551 ± 0.013
	FPA-GFZGSM	2.66 ± 0.08	103.27 ± 1.61	0.48 ± 0.08	288.89 ± 10.39	−0.580 ± 0.016
	FPA-JPLGSM	2.63 ± 0.06	101.36 ± 1.48	0.48 ± 0.06	295.40 ± 8.85	−0.563 ± 0.015

Due to differences in the start times of the GCM time-series estimated by different techniques, the annual and semi-annual phases of the SLR-based GCM estimates cannot be directly compared with those of the GRACE-based GCM estimates. To visually represent the dispersion of the GCM estimates, a phasor diagram illustrating the phases and amplitudes of the annual and semi-annual signals is shown in Fig. 7. In Fig. 7, both the phases and amplitudes of the GRACE-based GCM estimates are closely clustered, indicating a strong consistency. In contrast, the SLR-based GCM estimates show greater dispersion, but the Yu-SLR-weekly annual and semi-annual signals in the *Y* component almost coincide with those of the GRACE-based GCM estimates.

4.3 Analysis of other periodic signals

In addition to detecting annual and semi-annual signals, MSSA also separates many other periodic signals. Figs 8, 9, and 10 show these periodic signals detected by MSSA in the *X*, *Y* and *Z* components

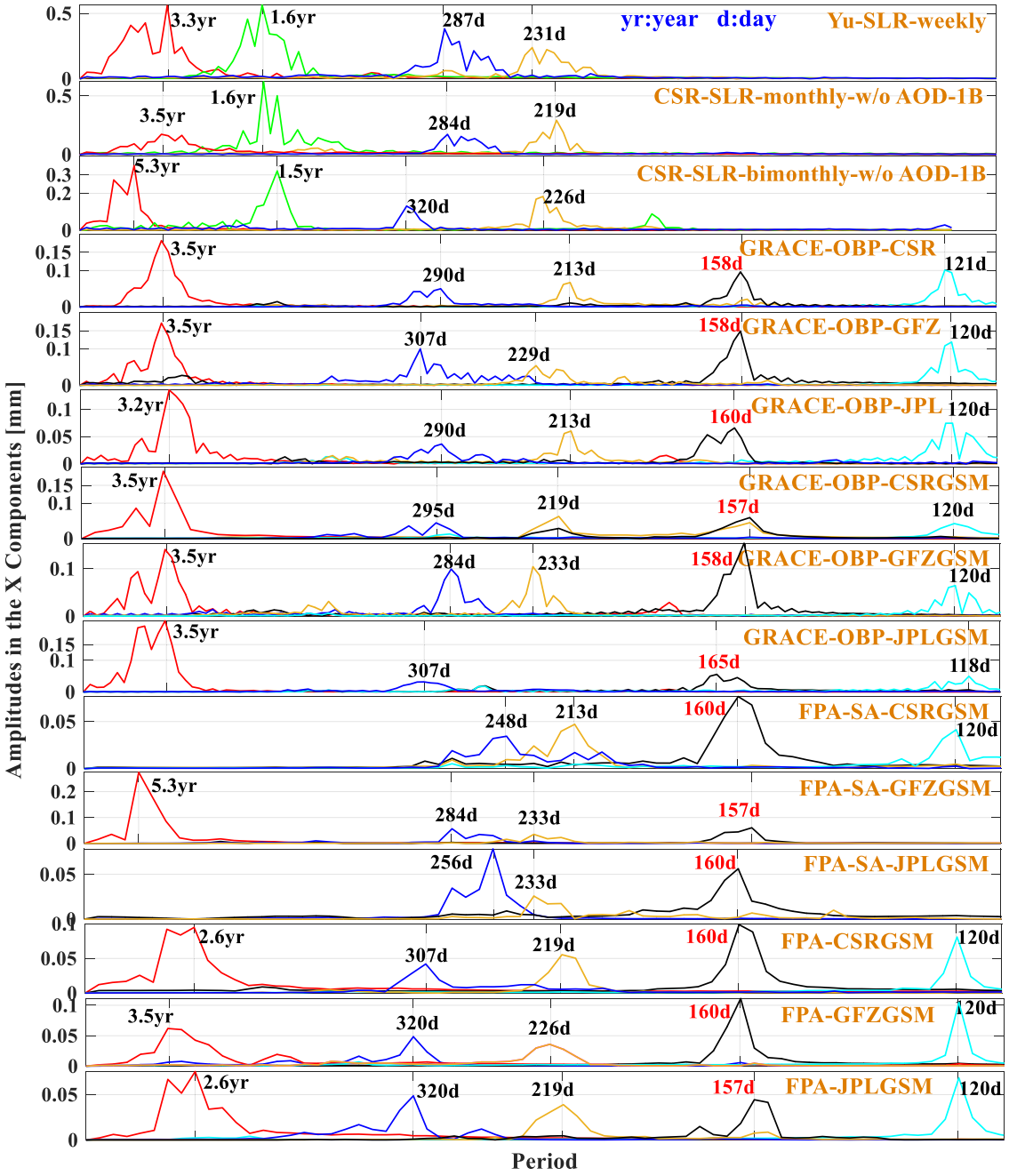

Figure 8. The periodic signals detected by MSSA in the X GCM components excluding the annual and semi-annual signals.

of the GCM time-series, respectively, excluding the annual and semi-annual signals. All SLR-based estimates contain a periodic draconitic signal close to 560 d (approximately 1.5 or 1.6 yr), and most SLR-based estimates have periodic signals of approximately 280 d and 220 d in all three components. These signals have been extensively discussed in related studies (Yu *et al.* 2021) in terms of the SLR-based GCM estimates and will not be elaborated further here. Interestingly, similar periodic signals were also detected in GRACE-based GCM estimates in this study, though the underlying geophysical factors require further investigation. Notably, unlike the study by Yu *et al.* (2021), which used SSA to identify periodic signals of 14.1 and 15.3 d in individual components, MSSA, by extracting common signals, does not detect these periodic signals from the *X*, *Y* and *Z* components within the first 30 reconstructed components. Instead, MSSA detects a previously undetected 120-d periodic signal in most GRACE-based GCM time-series, though this signal is absent in the FPA-SA-GFZGSM and FPA-SA-JPLGSM time-series. This 120-d signal reflects the variations in global precipitation (Chen *et al.* 1996), atmospheric circulation (Stan and Krishnamurthy 2019), and atmospheric and oceanic angular momentum (Nastula *et al.* 2011). Additionally, a 3- to 4-yr periodic signal was detected in most GCM time-series. In the *X* component, this signal is primarily observed as a 3.5-yr period, while in the *Y* and *Z* components, it may manifest as 3 or 4.2 yr due to

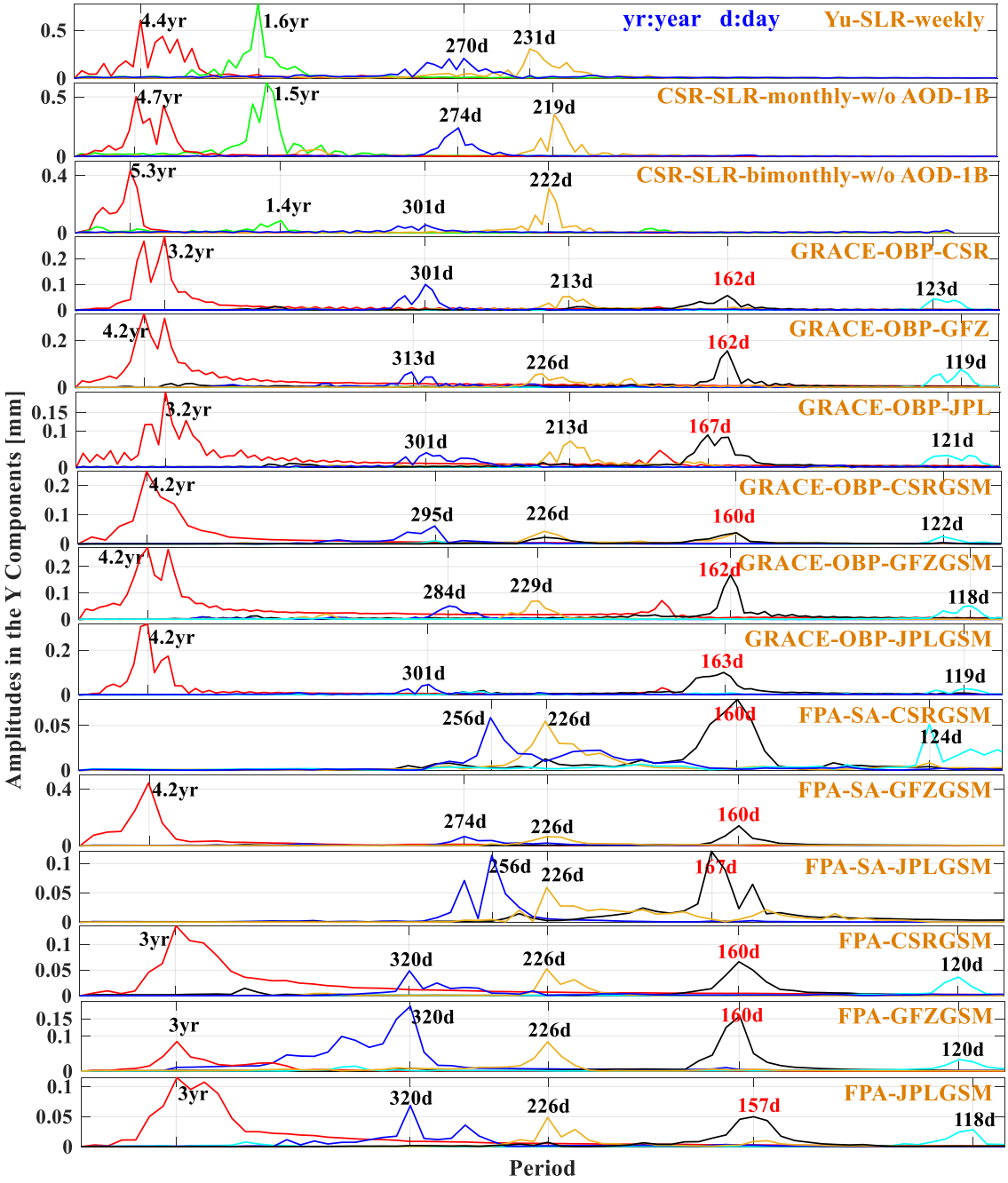

Figure 9. The periodic signals detected by MSSA in the Y GCM components excluding the annual and semi-annual signals.

sidelobe frequencies resulting from the coupling of sampling and signal frequencies. The geophysical origin of this signal is currently unclear, and its authenticity needs to be validated through geophysical mechanisms.

Among these periodic signals, the 160-d periodic signal captured our attention the most, as it was consistently detected in all GRACE-based GCM estimates (see Figs 8, 9, and 10). This inevitably brings to mind the extensive discussions regarding the unreliability of the C_{20} coefficient. Although the GRACE satellite, launched in 2002, and its successor, GRACE Follow-On, have provided global time-variable gravity fields with high spatial resolution, they have failed to provide a reliable C_{20} term (Cheng & Ries 2018) due to the presence of a 160-d periodic signal. Chen *et al.* (2009) identified this signal as a result of aliasing with the S_2 tide, which is particularly pronounced in high-latitude regions but also evident in other latitudes. This aliasing primarily arises from the relatively sparse coverage of satellite altimeter and tide gauge observations. Analyses of longer time-series data have demonstrated significant reductions in S_2 aliasing errors observed in some regions, inferring an improved separation between semi-annual hydrological effects and the 160-d S_2 signal. Despite continuous advancements

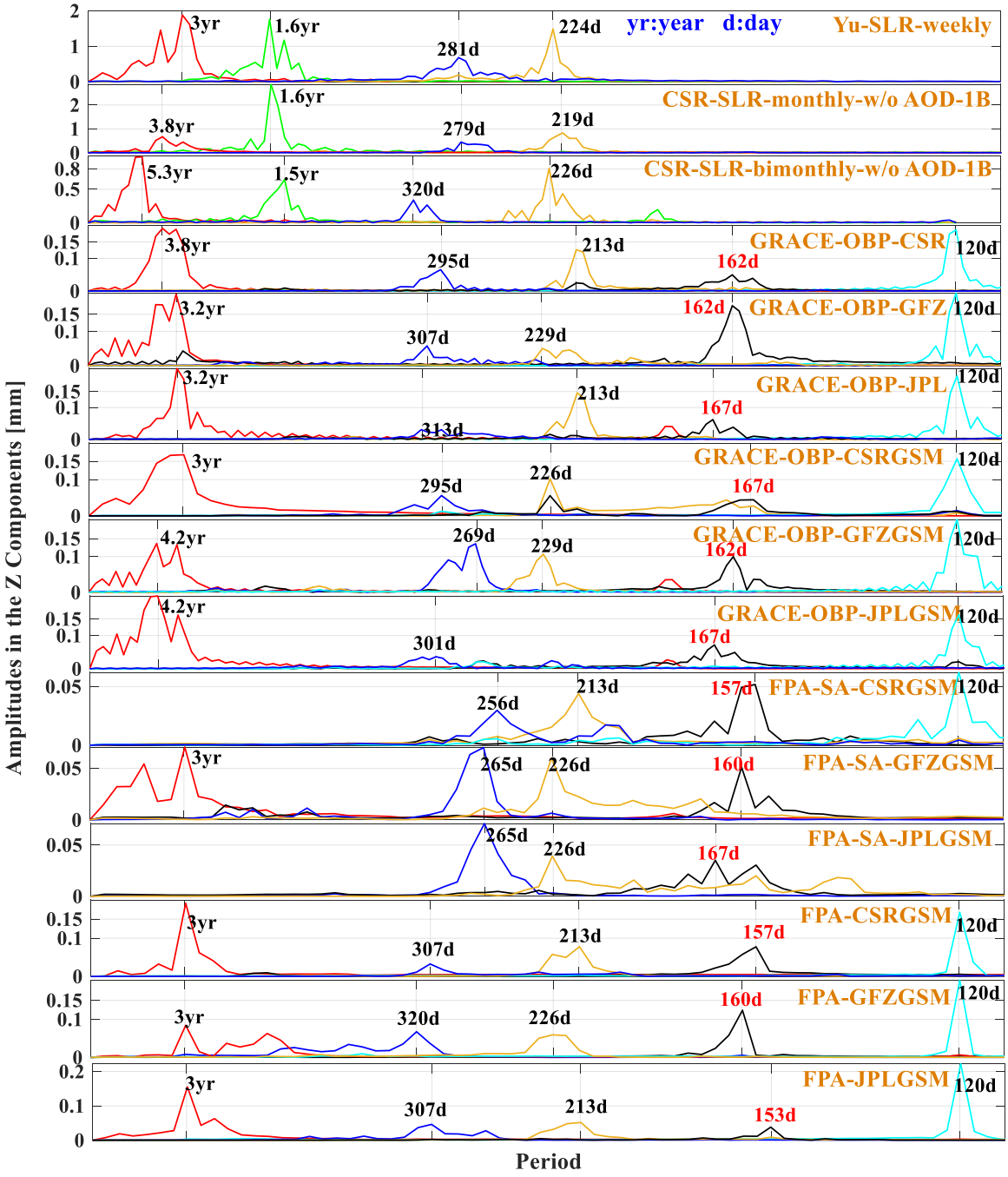

Figure 10. The periodic signals detected by MSSA in the Z GCM components excluding the annual and semi-annual signals.

in GRACE-related tidal models, aliasing remains an issue. Consequently, Cheng & Ries (2017) suggested that the 160-d anomaly in the GRACE C_{20} cannot be solely explained by S_2 tidal aliasing. Instead, it is related to temperature effects in the accelerometer data from the GRACE satellite. Subsequent improvements in addressing these temperature effects have enhanced the reliability of the C_{20}.

This phenomenon, along with our discovery of a 160-d periodic signal in all GRACE-based GCM estimates, sparked our research interest: where does this 160-d periodic signal originate? The GRACE-based estimates, using the GRACE-OBP (as described in eq. 3 by Sun *et al*. 2016) and FPA/FPA-SA (as described in eq. 1 by Sun *et al.* 2019) approaches, employ GRACE Earth's gravity field as input data. This motivated us to apply MSSA to analyse the SH coefficients with degree and order (d/o) not less than 2 (d/o $\geq$ 2, excluding C_{20}). Our analysis revealed that a significant approximately 160-d periodic signal was detected in each SH coefficient. This signal is likely related to half of the draconitic period for GRACE. The amplitudes of this period signal in the SH coefficients up to d/o 10 are depicted in Fig. 11. Notably, the amplitude decreases significantly for d/o coefficients higher than 10, dropping from the magnitude of 10^{-12} to 10^{-13}. Therefore, further analysis of SH coefficients with d/o greater than 10 is unnecessary. Additionally, we found it impossible to determine a definitive phase for the

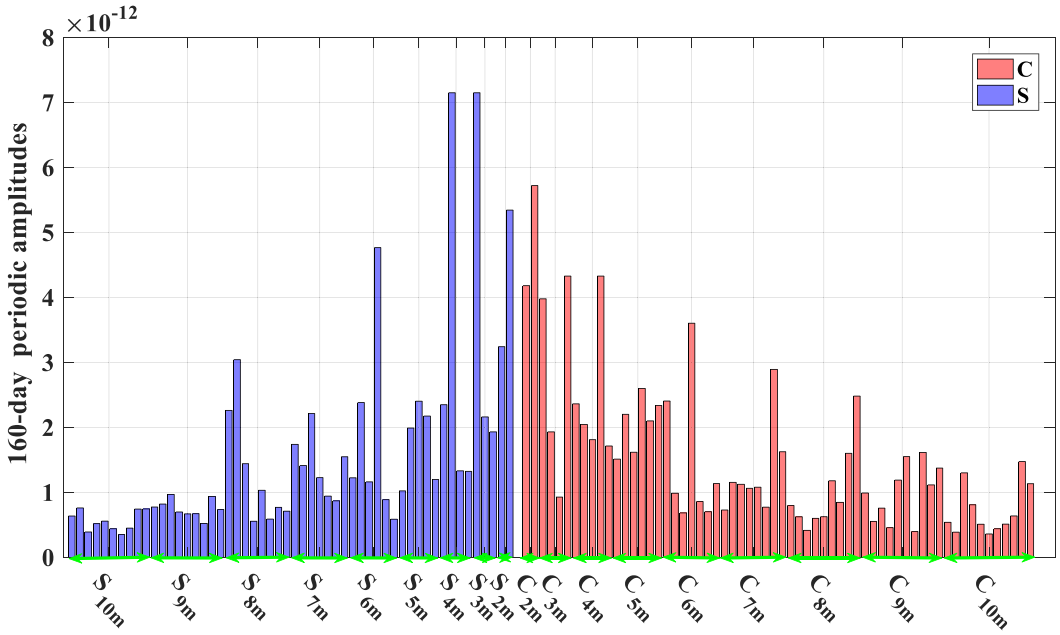

Figure 11. The amplitudes of the 160-d signals detected in the SH coefficients with degrees and orders not less than 2 (d/o $\geq$ 2, excluding C_{20}), and m representing the order of the SH coefficients.

160-d signals due to the continuously varying nature of the harmonic signals identified through MSSA and the fact that a single excitation source can produce SH coefficients (such as C_{20}, C_{21}, S_{21}, C_{30} and S_{32}) with different phases, each holding distinct geophysical meanings.

This study is the first to uncover that all SH coefficients exhibit a 160-d anomaly signal, emphasizing the need for further investigation into its underlying causes. Nevertheless, we are confident that this signal, detected in the GCM estimates derived from GRACE-based approaches, originates from these SH coefficients, thereby introducing a systematic error into the GCM estimates. This raises concerns about the reliability of GRACE-based GCM estimates for scientific research, highlighting the necessity for further validation.

Additionally, MSSA analysis was conducted on a 7-d SLR-based and twelve 30-d GRACE-based GCM estimates, identifying annual and semi-annual signals, as well as other signals with periods of approximately 3.5 yr, 220 d, and 280 to 320 d. These signals were also detected in the individual analyses of each GCM time-series (Figs 8, 9, and 10), confirming the overall consistency between the SLR-based and GRACE-based GCM time-series while emphasizing their unique characteristics.

4.4 Trend analysis

Fig. 6 clearly shows that the long-term trend is minimal, especially in the X component for the SLR-based GCM estimates. Since SLR-based GCM estimates represent the CM variations with respect to CF as defined by ITRF, no trends are expected during the periods contributing to the ITRF realization. However, due to differences in the choice of ITRF or error propagation, the actual SLR-based GCM estimates exhibit relatively small but different trends. As shown in Fig. 2, the SLR-based GCM time-series from 1994 to 2014 shows almost no trend. However, an obvious upward drift appears after 2014, coinciding with the implementation of the SLRF2014 reference frame. Interestingly, the trend in the SLR-based monthly GCMs from CSR contrasts with those of other GCM estimates. Meanwhile, the detrended bimonthly GCMs provided by CSR, shown in Fig. 5, indicate no trend as the detrended time-series is directly provided. The trends in the Y and Z components of the Yu-SLR-weekly and the AIUB-SLR-weekly GCM estimates (Sosnica *et al.* 2015; Zajdel *et al.* 2019a) are highly consistent, while the trend in the X component shows an opposite pattern. Furthermore, the AIUB-SLR-weekly GCM time-series was derived using ITRF2008, which has a slightly different origin compared to ITRF2014. Consequently, slight differences in trends may occur when different ITRF realizations are used (Altamimi *et al.* 2023).

Additionally, GRACE-based GCM estimates exhibit larger trends, especially in the Z component, due to GRACE's sensitivity to global mass changes such as GIA, ice melting and hydrological variations. Unlike SLR-based estimates, which are directly tied to ITRF and therefore expected to show minimal or no trends, GRACE-based estimates may exhibit secular non-zero trends because they are not directly linked to ITRF. Instead, the implementation of these GRACE-based methods, including GRACE-OBP and FPA/FPA-SA, relies on the geophysical models such as GIA or glacier melting (e.g. AIS and GrIS) rather than solely on direct GRACE satellite observations, which can introduce greater inaccuracies into GCM estimates. In contrast, SLR-based estimates are derived from direct satellite observational data, providing actual measurements.

5 DISCUSSIONS AND CONCLUSIONS

We use MSSA to investigate the time-scale characteristics of the GCM time-series estimated through various techniques, including SLR-based approaches (network shift and dynamic methods) and GRACE-based approaches (GRACE-OBP and FPA/FPA-SA methods). This analysis offers insights into the performance of each technique from the perspective of GCM signal analysis. Four types

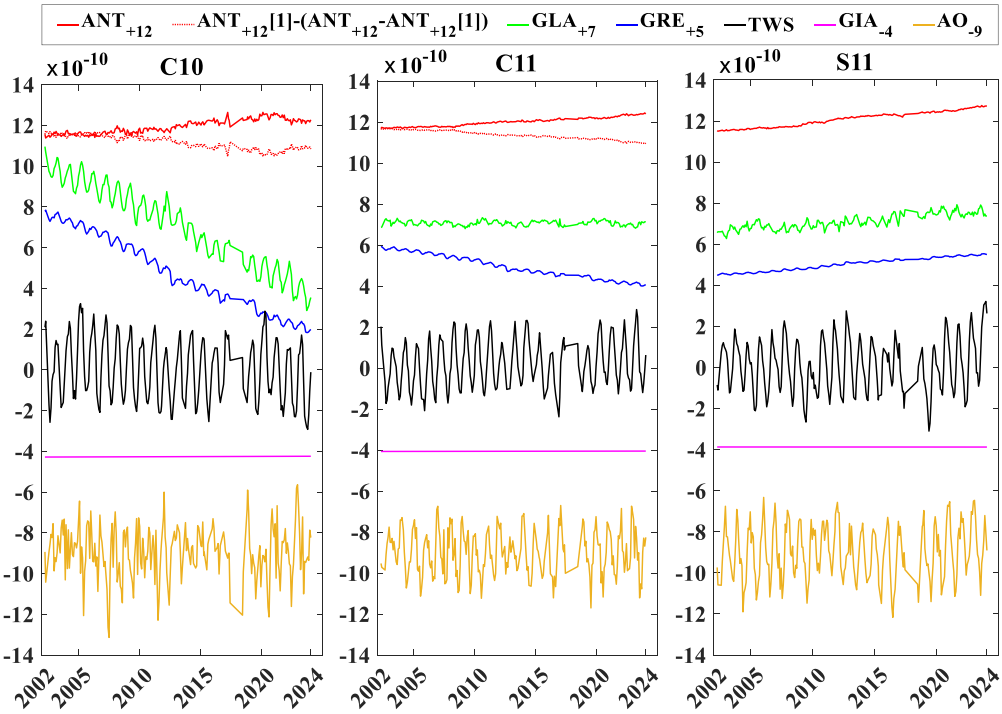

Figure 12. The contributions to GCM from various components of the Earth system calculated using the FPA method (from top to bottom: ANT, GLA, GRE, TWS, GIA and AO). The AO component is provided by the AOD-1B product. The subscripts indicate the positions shifted up and down on the vertical axis, and the red dashed line represents the position symmetrical to ANT for a more intuitive comparison of trend changes with GRE and GLA.

of GCM time-series were derived using different methods in this study.

The seasonal components of GRACE-based monthly GCM estimates closely align with those of SLR-based monthly GCM estimates, supporting their reliable application in seasonal correlation studies. However, the trends detected in GRACE-based monthly GCM estimates are significantly larger than those in SLR-based monthly and weekly GCM estimates. This discrepancy is primarily due to two factors: (1) SLR-based geocentre estimates do not exhibit a secular trend because they capture the CM variations with respect to the CF as defined by ITRF. In essence, the SLR-based GCM solutions reflect the motion relative to the ITR

F (or the SLR core network). Since the ITRF itself already describes the linear motion of the geocentre through station velocities, SLR-based GCM estimates are expected to capture only additional motions, such as seasonal variations. Significant trends are not anticipated in the SLR-based GCM results, though small trends may occur due to error propagation. (2) The reliance of GRACE-based approaches on geophysical models, particularly the GIA and glacier melting models, tends to amplify trends, especially in the Z component. Zhang & Sun (2018) demonstrated that the atmosphere and ocean (AO) components account for 54, 62 and 25 per cent of the observed geocentre motion variances in the X, Y and Z components, respectively. The terrestrial water storage (TWS) component alone explains 42, 32, and 39 per cent of the observed variances. Further research is required to understand the contributions of GIA and glacier melting to the GCM. The FPA-CSRGSM series, derived using the FPA approach, provides insights into the contributions of various Earth system components, including the Antarctic (ANT) and Greenland (GRE) ice sheets, TWS, GIA, continental glaciers (GLA) and AO effects removed by GSM (see Fig. 12). The results indicate that the geocentre seasonal motion is mainly driven by TWS and AO components, with GLA and GRE also contributing significantly to the Z (C_{10}) component. The trend component is primarily driven by the melting of polar ice sheet melting. Notably, except for the Y component (S_{11}), the mass redistribution from GRE (blue line) and the ANT (red line) ice sheets affects the GCM in opposite components, with GRE having a stronger influence, as evidenced by the slope comparison of the red dashed line and the blue line (Sun *et al.* 2019). While GIA also contributes to long-term trend changes, its effect is relatively small based on FPA results and requires further investigation for confirmation. Overall, while the trends in GRACE-based GCM estimates are obtainable, additional validation is essential to ensure their accuracy.

Additionally, the GCM estimated using GRACE-based approaches can be considered to maintain consistency among SH coefficients to some extent, as they derive lower-degree and order SH coefficients from higher-degree and order ones. However, these methods inadvertently introduce a 160-d periodic signal. While extensive research has been conducted on the C_{20} coefficient, there remains a significant gap in the discussion or exploration of this periodicity in other SH coefficients. This study provides valuable insights into mitigating the 160-d periodic signal in the determination of Earth's gravity field using GRACE satellites.

Overall, each technique for estimating the GCM has its distinct strengths and limitations. The network shift and dynamic method mainly rely on the locations of SLR stations and satellite orbit data, making them particularly suitable for long-term and high-precision GCM estimates. Longer time-series further enhance their ability to detect and separate signals. In contrast, GRACE-based methods (e.g. GRACE-OBP and FPA/FPA-SA) use geophysical models such

as the GRACE gravity field model, OBP, glacier melting models and GIA, but they heavily depend on data processing and modelling techniques. A comparative analysis of these methods enables the identification of their respective strengths, helping to improve the accuracy and reliability of GCM estimates. Notably, the SLR-derived GCM estimates, based on direct observations, can serve as a benchmark for validating and calibrating GRACE-derived products. Optimizing GRACE-based GCM estimates, particularly by addressing systematic errors, such as the unintended 160-d periodicity introduced by geophysical models (e.g. the GRACE gravity field model), is essential for advancing geodynamic and geophysical research.

ACKNOWLEDGMENTS

This work was primarily supported by the National Natural Science Foundation of China (Project Nos. 42304099, 42171426 and 41801393). The authors express their gratitude to the International Laser Ranging Service (ILRS) for providing LAGEOS1/2 observations, CSR for supplying GRACE data and International Center for Global Earth Models (ICGEM) for the Earth's gravity field models used for estimating geocentre motion. Additionally, the authors thank the Astronomical Institute, University of Bern, for the weekly GCM time-series, Ries (2016) of CSR for the monthly and bimonthly GCM solutions and CSR, GFZ and JPL for providing GRACE-OBP GCM estimates for validation purposes.

CONFLICT OF INTEREST

The authors declare no conflict of interest. The authors confirm that this work is original and has not been published elsewhere, nor is it currently under consideration for publication elsewhere. No conflict of interest exits in the submission of this manuscript, and manuscript is approved by all authors for publication.

DATA AVAILABILITY

The LAGEOS1/2 observations were derived from the ILRS (available at https://edc.dgfi.tum.de/pub/slr/data/), the GRACE data (accessible at http://www2.csr.utexas.edu/grace/) and the Earth's gravity field models from ICGEM (https://icgem.gfz-potsdam.de/sl/temporal) are utilized for estimating the GCM. Additionally, the weekly GCM time-series from the Astronomical Institute, University of Bern (available at http://ftp.aiub.unibe.ch/GRAVITY/GEOCENTER), the monthly and bimonthly GCM solutions from Ries (2016) of the Center for Space Research (CSR) (accessible at https://filedrop.csr.utexas.edu/pub/slr/geocenter/), and the GRACE-OBP GCM estimates provided by CSR, GFZ and JPL (available at https://podaac.jpl.nasa.gov/gravity/grace-documentation#TechnicalNotes) are used for validation purposes. The ocean and atmospheric components are reduced using the AOD products (available at ftp://isdcftp.gfz-potsdam.de/grace-fo/Level-1B/GFZ/AOD/).

REFERENCES

Altamimi, Z., Rebischung, P., Collilieux, X., Métivier, L. & Chanard, K., 2023. ITRF2020: an augmented reference frame refining the modeling of nonlinear station motions, *J. Geod.,* **97**(5), 47, doi: 10.1007/s00190-023-01738-w.

Bergmann-Wolf, I., Zhang, L. & Dobslaw, H., 2014. Global eustatic sea-level variations for the approximation of geocenter motion from GRACE, *J. Geod. Sci.,* **4**(1), 37–48.

Chen, J., Cazenave, A., Dahle, C., Llovel, W., Panet, I., Pfeffer, J. & Moreira, L., 2022. Applications and challenges of GRACE and GRACE follow-on satellite gravimetry, *Surv. Geophys.,* **43**(1), 305–345.

Chen, J., Tapley, B., Seo, K.-W., Wilson, C. & Ries, J., 2019. Improved quantification of global mean ocean mass change using GRACE satellite gravimetry measurements, *Geophys. Res. Lett.,* **46**(23), 13 984–13 991.

Chen, J., Tapley, B., Wilson, C., Cazenave, A., Seo, K.-W. & Kim, J.-S., 2020. Global ocean mass change from GRACE and GRACE follow-on and altimeter and argo measurements, *Geophys. Res. Lett.,* **47**(22), e2020GL090656, doi:10.1029/2020GL090656.

Chen, J.L., Wilson, C.R., Eanes, R.J. & Nerem, R.S., 1999. Geophysical interpretation of observed geocenter variations, *J. Geophys. Res. Solid Earth,* **104**(B2), 2683–2690.

Chen, J.L., Wilson, C.R. & Seo, K.W., 2009. S2 tide aliasing in GRACE time-variable gravity solutions, *J. Geod.,* **83,** 679–687.

Chen, T.-.C., Pfaendtner, J., Chen, J.-.M. & Wikle, C.K., 1996. Variability of the global precipitable water with a timescale of 90–150 days, *J. Geophys. Res. Atmos.,* **101**(D5), 9323–9332.

Cheng, M., 2024. An updated estimate of geocenter variation from analysis of SLR data, *Remote Sens.,* **16**(7), 1189, doi:10.3390/rs16071189.

Cheng, M. & Ries, J.C., 2017. The unexpected signal in GRACE estimates of C20, *J. Geod.,* **91**(8), 897–914.

Cheng, M. & Ries, J.C., 2018. Decadal variation in Earth's oblateness (J2) from satellite laser ranging data, *Geophys. J. Int.,* **212**(2), 1218–1224.

Cheng, M., Tapley, B.D. & Ries, J.C., 2013b. Deceleration in the Earth's oblateness, *J. Geophys. Res. Solid Earth,* **118**(2), 740–747.

Cheng, M.K., Ries, J.C. & Tapley, B.D., 2013a. Geocenter Variations from Analysis of SLR Data, *Reference Frames for Applications in Geosciences,* pp. 19–25, Springer, Berlin.

Dong, D., Dickey, J.O., Chao, Y. & Cheng, M.K., 1997. Geocenter variations caused by atmosphere, ocean and surface ground water, *Geophys. Res. Lett.,* **24**(15), 1867–1870.

Glaser, S., König, R., Neumayer, K.H., Balidakis, K. & Schuh, H., 2019. Future SLR station networks in the framework of simulated multi-technique terrestrial reference frames, *J. Geod.,* **93**(11), 2275–2291.

Guo, J.Y., Han, Y.B. & Hwang, C.W., 2008. Analysis on motion of Earth's center of mass observed with CHAMP mission, *Sci. China-Phys. Mech. Astron.,* **51**(10), 1597–1606.

Hassani, H., 2007. Singular spectrum analysis: methodology and comparison, *J. Data Sci.,* **05**(2), 239–257.

Ji, K., Shen, Y., Chen, Q. & Wang, F., 2023. Extended singular spectrum analysis for processing incomplete heterogeneous geodetic time series, *J. Geod.,* **97**(8), 74, doi:10.1007/s00190-023-01764-8.

Jin, X., Liu, X., Guo, J. & Shen, Y., 2021. Analysis and prediction of polar motion using MSSA method, *Earth Planets Space,* **73,** 1–13.

Kosek, W., Popiński, W., Wnęk, A., Sośnica, K. & Zbylut-Górska, M., 2020. Analysis of systematic errors in geocenter coordinates determined from GNSS, SLR, DORIS, and GRACE, *Pure appl. Geophys.,* **177**(2), 867–888.

Loomis, B.D., Rachlin, K.E. & Luthcke, S.B., 2019. Improved Earth oblateness rate reveals increased ice sheet losses and mass-driven sea level rise, *Geophys. Res. Lett.,* **46**(12), 6910–6917.

Loomis, B.D., Rachlin, K.E., Wiese, D.N., Landerer, F.W. & Luthcke, S.B., 2020. Replacing GRACE/GRACE-FO with satellite laser ranging: impacts on antarctic ice sheet mass change, *Geophys. Res. Lett.,* **47**(3), e2019GL085488, doi:10.1029/2019GL085488.

Métivier, L., Rouby, H., Rebischung, P. & Altamimi, Z., 2020. ITRF2014, Earth figure changes, and geocenter velocity: implications for GIA and recent ice melting, *J. Geophys. Res.: Solid Earth,* **125**(2), e2019JB018333, doi: 10.1029/2019JB018333.

Nastula, J., Paśnicka, M. & Kołaczek, B., 2011. Comparison of the geophysical excitations of polar motion from the period: 1980.0–2009.0, *Acta Geophys.,* **59,** 561–577.

Nie, Y., Chen, J. & Peng, D., 2024. Global ocean mass change estimation using low-degree gravity field from satellite laser ranging, *Geophys. Res. Lett.,* **51**(11), e2024GL109717.

Richard Peltier, W., Argus, D.F. & Drummond, R., 2018. Comment on "an assessment of the ICE-6G_C (VM5a) glacial isostatic adjustment model" by Purcell et al., *J. Geophys. Res. Solid Earth,* **123**(2), 2019–2028.

Ries, J.C., 2016. Reconciling estimates of annual geocenter motion from space geodesy, In *Proceedings of the 20th International Workshop on Laser Ranging,* Potsdam, Germany, pp. 10–14, http://ilrs.gsfc.nasa.gov/lw20/docs/2016/papers/14-Ries_paper.pdf.

Rietbroek, R., Brunnabend, S.-E., Kusche, J., Schröter, J. & Dahle, C., 2016. Revisiting the contemporary sea-level budget on global and regional scales, *Proc. Natl. Acad. Sci. USA,* **113**(6), 1504–1509.

Shen, Y., Wang, F. & Chen, Q., 2021. Weighted multichannel singular spectrum analysis for post-processing GRACE monthly gravity field models by considering the formal errors, *Geophys. J. Int.,* **226**(3), 1997–2010.

Sośnica, K., Jäggi, A., Meyer, U., Thaller, D., Beutler, G., Arnold, D. & Dach, R., 2015. Time variable Earth's gravity field from SLR satellites, *J. Geod.,* **89**(10), 945–960.

Sośnica, K., Jäggi, A., Thaller, D., Beutler, G. & Dach, R., 2014. Contribution of Starlette, Stella, and AJISAI to the SLR-derived global reference frame, *J. Geod.,* **88**(8), 789–804.

Spatar, C.B., 2016. Observability and Estimation of Geocentre Motion Using Multi-satellite Laser Ranging, *PhD Dissertation,* Newcastle University, England.

Stan, C. & Krishnamurthy, V., 2019. Intra-seasonal and seasonal variability of the Northern Hemisphere extra-tropics, *Clim. Dyn.,* **53**(7), 4821–4839.

Sun, Y., Ditmar, P. & Riva, R., 2016b. Observed changes in the Earth's dynamic oblateness from GRACE data and geophysical models, *J. Geod.,* **90**(1), 81–89.

Sun, Y., Ditmar, P. & Riva, R., 2017. Statistically optimal estimation of degree-1 and C20 coefficients based on GRACE data and an ocean bottom pressure model, *Geophys. J. Int.,* **210**(3), 1305–1322.

Sun, Y., Li, Y., Guo, X. & Guo, J., 2023. Estimating C 30 coefficients for GRACE/GRACE-FO time-variable gravity field models using the GRACE-OBP approach, *J. Geod.,* **97**(3), 20.

Sun, Y., Riva, R. & Ditmar, P., 2016a. Optimizing estimates of annual variations and trends in geocenter motion and J2 from a combination of GRACE data and geophysical models, *J. Geophys. Res. Solid Earth,* **121**(11), 8352–8370.

Sun, Y., Riva, R., Ditmar, P. & Rietbroek, R., 2019. Using GRACE to explain variations in the Earth's oblateness, *Geophys. Res. Lett.,* **46**(1), 158–168.

Swenson, S., Chambers, D. & Wahr, J., 2008. Estimating geocenter variations from a combination of GRACE and ocean model output, *J. Geophys. Res. Solid Earth,* **113**(B8), doi:10.1029/2007JB005338.

Tamisiea, M.E., Hill, E.M., Ponte, R.M., Davis, J.L., Velicogna, I. & Vinogradova, N.T., 2010. Impact of self-attraction and loading on the annual cycle in sea level[J], *J. Geophys. Res. Oceans,* **115**(C7), doi:10.1029/2009JC005687.

Tapley, B.D., Bettadpur, S., Watkins, M. & Reigber, C., 2004. The gravity recovery and climate experiment: mission overview and early results, *Geophys. Res. Lett.,* **31**(9), doi:10.1029/2004GL019779.

Wang, F., Shen, Y., Chen, Q. & Wang, W., 2021. Bridging the gap between GRACE and GRACE follow-on monthly gravity field solutions using improved multichannel singular spectrum analysis, *J. Hydrol.,* **594**(2019), 125 972, doi:10.1016/j.jhydrol.2021.125972.

Yu, H., Sośnica, K. & Shen, Y., 2021. Separation of geophysical signals in the LAGEOS geocentre motion based on singular spectrum analysis, *Geophys. J. Int.,* **225**(3), 1755–1770.

Zajdel, R., Sośnica, K., Dach, R., Bury, G., Prange, L. & Jäggi, A., 2019b. Network effects and handling of the geocenter motion in multi-GNSS processing, *J. Geophys. Res. Solid Earth,* **124**(6), 5970–5989.

Zajdel, R., Sośnica, K., Drożdżewski, M., Bury, G. & Strugarek, D., 2019a. Impact of network constraining on the terrestrial reference frame realization based on SLR observations to LAGEOS, *J. Geod.,* **93**(11), 2293–2313.

Zannat, U.J. & Tregoning, P., 2017a. Estimating network effect in geocenter motion: theory, *J. Geophys. Res. Solid Earth,* **122**(10), 8360–8375.

Zannat, U.J. & Tregoning, P., 2017b. Estimating network effect in geocenter motion: applications, *J. Geophys. Res. Solid Earth,* **122**(10), 8347–8359.

Zhang, H. & Sun, Y., 2018. Climate-driven seasonal geocenter motion during the GRACE period, *Acta Geophys.,* **66,** 223–232.

Zhang, L., Shen, Y., Chen, Q. & Wang, F., 2023. Influence factors and mechanisms of 2015–2016 extreme flood in Pearl River Basin based on the WSDI from GRACE, *J. Hydrol. Reg. Stud.,* **47,** 101 376.

Zhou, M., Guo, J., Liu, X., Shen, Y. & Zhao, C., 2020. Crustal movement derived by GNSS technique considering common mode error with MSSA, *Adv. Space Res.,* **66**(8), 1819–1828.